Research Article

Harun Sepetcioglu, Lubomír Lapčík*, Barbora Lapčíková, Martin Vašina, David Hui, Martin Ovsík, Michal Staněk, Yousef Murtaja, Libor Kvítek, Tereza Lapčíková, and Oldřich Zmeškal

Improved mechanical properties of graphene-modified basalt fibre–epoxy composites

https://doi.org/10.1515/ntrev-2024-0052
received November 10, 2023; accepted June 11, 2024

Abstract: In industrial applications, the potential of basalt fibre-reinforced polymer (BFRP) composite pipes as a compelling alternative to glass and carbon fibre-reinforced composite pipes is recognized. Their high recyclability makes them a viable option for aerospace, marine, and automotive applications. In this study, a comparison is made between the mechanical properties of virgin basalt–epoxy composite pipes and graphene-modified counterparts. To conduct the experiments, pipe section specimens were prepared using a flex grinding machine. Graphene nanoplatelets (GnPs), serving as an exceptional reinforcing material, were uniformly incorporated into the basalt–epoxy composites at a specific concentration. The inclusion of these nanoplatelets resulted in significant changes in mechanical stiffness compared to the virgin basalt–epoxy composite pipes. A series of tests, including uniaxial tensile, Charpy impact, microhardness, Shore D hardness, uniaxial 3-point bending, and dynamic displacement transmissibility tests, were carried out to assess the mechanical properties of both graphene-reinforced and virgin basalt–epoxy pipes. The findings indicated that the pure basalt–epoxy composite exhibited lower ductility compared to the graphene basalt–epoxy composites after undergoing uniaxial mechanical loading. Non-destructive dynamic mechanical vibration testing was used to investigate the complex mechanical response of the materials under examination. The observed complex frequency-dependent responses reflected the mutual ductile/brittle mechanical performance of the developed composites.

Keywords: graphene-modified basalt fibres, composite pipes, epoxy polymer, mechanical testing

*** Corresponding author: Lubomír Lapčík,** Department of Physical Chemistry, Faculty of Science, Palacky University, 17. Listopadu 12, 771 46, Olomouc, Czech Republic; Faculty of Technology, Tomas Bata University in Zlin, Vavreckova 5669, 760 01, Zlin, Czech Republic, e-mail: lapcikl@seznam.cz
Harun Sepetcioglu: Department of Metallurgy and Materials Engineering, Technology Faculty, Selçuk University, Konya, 42075, Turkey
Barbora Lapčíková: Department of Physical Chemistry, Faculty of Science, Palacky University, 17. Listopadu 12, 771 46, Olomouc, Czech Republic; Faculty of Technology, Tomas Bata University in Zlin, Vavreckova 5669, 760 01, Zlin, Czech Republic
Martin Vašina: Faculty of Technology, Tomas Bata University in Zlin, Vavreckova 5669, 760 01, Zlin, Czech Republic; Department of Hydromechanics and Hydraulic Equipment, Faculty of Mechanical Engineering, VŠB-Technical University of Ostrava, 17. Listopadu 15/2172, 708 33, Ostrava-Poruba, Czech Republic
David Hui: Department of Mechanical Engineering, Composite Material Research Laboratory, University of New Orleans, 2000 Lakeshore Dr, New Orleans, LA, 70148, United States of America
Martin Ovsík, Michal Staněk: Faculty of Technology, Tomas Bata University in Zlin, Vavreckova 5669, 760 01, Zlin, Czech Republic
Yousef Murtaja, Libor Kvítek: Department of Physical Chemistry, Faculty of Science, Palacky University, 17. Listopadu 12, 771 46, Olomouc, Czech Republic
Tereza Lapčíková, Oldřich Zmeškal: Faculty of Chemistry, Institute of Physical and Applied Chemistry, Brno University of Technology, Purkynova 118, Brno, 61200, Czech Republic

1 Introduction

Composite structures are tailored to achieve specific properties suitable for anticipated environments [1,2]. Fibre-reinforced epoxy resin composites have emerged as an advanced material choice for pipe fabrication, surpassing traditional metal pipes in applications such as underground material and fluid transport, including oil, natural gas, wastewater, thermal water, and drinking water. The diverse range of fluids and their associated pressures can significantly impact the material performance. Nevertheless, thanks to their exceptional corrosion resistance, wear resistance, and high strength-to-weight ratio, fibre-reinforced epoxy resin composites offer a substantial advantage over conventional pipe materials [3–6].

Pressure pulsations, arising from centrifugal pumps or reciprocating compressors in pipeline systems, have well-known detrimental effects on industrial applications. Hydraulic pumps (*e.g.*, centrifugal, piston, or gear pumps), operating on positive displacement principles, inherently produce output

flow pulsations leading to pressure pulsations upon encountering liquid resistance. These pulsations traverse the pipeline, causing vibration, noise, damage, and potential safety hazards such as pipes rupture or damage of other components in hydraulic systems [7–11].

Basalt, a natural and environmentally friendly material, is used to produce basalt fibres (BFs) [12]. BFs are more recyclable compared to glass fibres, making them an excellent choice for various applications, including marine, automotive, and aerospace industries where a basalt fibre-reinforced polymer (BFRP) is used [13,14]. They show promise as replacements for glass and carbon fibres due to their exceptional recyclability. BFs have been proven to be non-toxic and non-carcinogenic. These fibres are created by drawing a natural ore through a platinum–rhodium alloy melted at high temperatures [15]. They are cost-effective and possess outstanding properties, including minimal moisture absorption, high-temperature resistance, corrosion resistance, sound absorption, and high strength [16–18]. Basalt's rough surface promotes strong adhesion to the polymer matrix, resulting in robust interfaces. Moreover, BFs exhibit a higher elongation percentage compared to carbon and glass fibres [19].

Epoxy resins serve as the matrix in composite fabrication, offering desirable characteristics such as low shrinkage during curing, excellent heat and chemical resistances, and high strength. However, they have a brittle structure [20–22].

Hybrid nanocomposites are typically fabricated by embedding two or more reinforcement materials within the host matrix. This combination enhances specific features, such as ductility, elastic modulus, strength, lightweight properties, and flame retardancy, providing the material with tailored superior properties [23–25].

Mechanical and thermal conductivity properties of polymers can be significantly enhanced by introducing carbon-based nano-sized reinforcements, including fullerene [26], carbon nanofibers [27,28], carbon nanotubes [29], and graphene [30].

The discovery of graphene has opened up new avenues for research as it is being incorporated into various composite structures to enhance their properties. Graphene was first isolated and characterized in 2004 by researchers at the University of Manchester (Manchester, UK), using adhesive tape to separate graphite into individual layers of carbon. A decade later, graphene-enhanced composite applications, from aramid nanofiber-reinforced supercapacitors for electric vehicle batteries to aerospace composite tooling and cryogenic pressure vessels, made the headlines. While the material has been commercially available for about a decade, its path to commercialization has significantly accelerated over the past couple of years, with over 2,300 graphene-related patents approved in the last 12 months, according to the Graphene Council (Manchester, UK).

The hexagonally structured single layer of carbon atoms offers extraordinary properties, such as a remarkable thickness of 0.334 nm, a vast specific surface area of approximately 2,600 m^2/g, high electron mobility at 200,000 cm^2/Vs, thermal conductivity ranging from 3,000 to 5,000 W/mK, exceptional optical transparency at 97.4%, and formidable mechanical strength with a Young's modulus of elasticity of 1 TPa [31]. These unique properties have opened doors to a diverse range of applications, including energy storage, electronics, healthcare, and construction, with graphene playing a pivotal role in enhancing various material and device performances [32–34], *e.g.*, filament-wounded BFRP solid particle erosion property enhancement by the reinforcement of non-functionalized GnPs at a concentration of 0.25% [35].

Graphene nanoplatelets (GnPs) integrated into an epoxy matrix exhibit excellent mechanical properties. The non-isotropic nature of a composite pipe reinforced with GnPs contributes to the enhancement of its mechanical properties, effectively minimizing potential damage from static and variable loads encountered during service conditions [30]. In practical engineering applications, particularly in the design of composite pressure vessels, rocket engine casings in aerospace, transportation of various fluids, safe conveyance and storage of chemicals, marine and offshore structures, penstock applications in hydropower projects, infrastructure projects like bridges and tunnels, cost-effective solutions for agricultural water distribution, and in mining operations for the transport of abrasive materials, the consideration of mechanical loads, both static and variable, holds a paramount significance. The ground-breaking aspect of composite pipes lies in their capacity to amalgamate the robustness of conventional materials with heightened corrosion resistance and prolonged durability. This quality renders GnP-reinforced composite pipes exceptionally well suited for a diverse array of industries and applications [30].

Several studies have been conducted to clarify the influence of GnPs on the mechanical properties of composite structures made from BFs, specifically in plate and pipe configurations. Sepetcioglu *et al.* [34] investigated the fatigue behaviour of basalt–epoxy composite pressure vessels with the incorporation of GnPs. According to their research, the addition of a small amount of GnPs improved the fatigue life of basalt–epoxy composite pressure vessels [34]. Madhukar and Drzal conducted a study on the low-velocity impact behaviour of twill basalt–epoxy composites by incorporating GnPs. The results indicated that the presence of GnPs in the BEC matrix increases low-velocity impact resistance by reducing absorbed energy during

rebound and increasing the contact angle [36]. Bulut investigated the enhancement of interlaminar shear strength, which subsequently improved the flexural and tensile properties through the addition of GnPs to the composite [37]. Boehm explored the mechanical properties of basalt–epoxy composite laminates with the incorporation of GnPs. The findings revealed that adding 0.1 wt% of GnPs to the composite significantly enhanced the bonding strength at the interface, leading to improved mechanical properties [38].

It is well established that graphene is an exceptional material for enhancing composite mechanical properties. In this study, the impact of GnPs incorporated into basalt–epoxy composites on material's mechanical properties was investigated, with a particular focus on their suitability for pipe applications. The comprehensive mechanical characterization of basalt composite pipes, enhanced with GnPs, is imperative prior to their broad utilization across diverse industries. This necessitates a thorough series of fundamental tests to ascertain their mechanical properties. Therefore, static and dynamic mechanical properties (tensile, bending, micro/nanohardness, unnotched fracture toughness, and vibration damping measurements) of graphene-modified BF–epoxy composite pipes manufactured by the filament winding method were studied. These mechanical tests in an academic context provide a holistic understanding of the composite pipe performance, aiding in material optimization and design for specific industrial needs, ensuring reliability, safety, and longevity.

2 Materials and methods

The unreinforced (Sample 1) and reinforced (Sample 2) BFRP composite pipes (outer diameter of 76 mm and 1 m length) were fabricated using the filament winding technique, as described by Sepetcioglu *et al.* [34]. The pipe's wall thickness was of 2 mm. EPIKOTE 828 LVEL bisphenol and EPIKURE 866 hardener agents were chosen as the epoxy resin system (Hexion, Inc., Columbus, Ohio, USA), with monofilament 400 tex BFs measuring 13 μm in diameter (Kamenny Vek, Inc., Dubna, Russian Federation). For epoxy modification, non-functionalized GnPs with a surface area of 800 g/m^2, a layer thickness ranging from 3 to 7 nm, an average layer width of 1.5 μm, and a purity of 99.9% were used as nanoreinforcements (Nanografi Nano Technology, Ankara, Turkey). Photographs of cutouts of tested composite pipes are shown in Figure S1. From these pipes, individual testing specimens were prepared for each testing methodology used in this study as described below (Figure 1).

Figure 1: Photograph of cutouts of tested composite pipes.

To incorporate the GnPs into the polymer matrix, a series of steps were followed. Initially, the GnPs were organized to achieve the desired weight ratio and were then introduced into the pure epoxy resin. The mixture of GnPs and epoxy resin was mechanically stirred for a period of 10–15 min, ensuring the initial dispersion of the GnPs throughout the epoxy matrix. Subsequently, the GnPs and epoxy resin mixture underwent ultrasonic mixing for 30 min to achieve a consistent distribution of GnPs within the epoxy matrix. This ultrasonic process introduced high-frequency sound waves to enhance the uniformity of GnPs, ensuring their even distribution throughout the epoxy [30].

During the winding process, BFs were passed through a drum to allow the impregnation of the GnP/epoxy mixture, ensuring the comprehensive saturation of the BFs with the GnP/epoxy matrix. In this study, a BFRP composite pipe reinforced with 0.25 wt% GnPs (based on our previous experimental optimization) was considered [34].

2.1 Scanning electron microscopy (SEM) analysis

An Axia ChemiSEM scanning electron microscope (Thermo Fisher Scientific, Inc., Seattle, USA) was used for SEM analysis of the fractured surfaces after uniaxial tensile testing. SEM measurements were performed at an accelerating voltage of 2 kV. No coatings of the specimens were used in the experiments.

2.2 Uniaxial tensile testing

A Universal Testing Machine Autograph AGS-100 Shimadzu (Kyoto, Japan) and a Zwick 1456 multipurpose tester (Zwick Roell, Ulm, Germany) equipped with a Compact Thermostatic Chamber TCE Series were used for tensile testing of virgin and graphene-reinforced specimens. All measurements were recorded according to ČSN EN ISO 527-1 and ČSN EN ISO 527-2 standards. Samples were cut by a flex grinding machine GWS 7-125 (Robert Bosch, JSC, Gerlingen, Germany) in dimensions of (25 × 200 × 2) mm (width × length × thickness). These pipe strip specimens, also referred to as pipe section specimens, exhibited curvature on both their inner and outer surfaces [39–41]. They were affixed using hydraulic flat jaws. However, it should be mentioned that plastic deformation of the pipe strip specimens at the holding area position can be induced by this clamping procedure. A snapshot photograph of the used uniaxial tensile testing instrument is shown in Figure S2.

Experimental measurements were performed at the room temperature of 25°C with 5 mm/min (Shimadzu instrument) and 10 mm/min (Zwick instrument) strain rates. Young's modulus of elasticity (E) and the elongation at maximum tensile force (dL_{max}) were obtained from the stress–strain dependency plots. Each experiment was repeated 10×, and mean values and standard deviations of the measured quantities were subsequently calculated.

2.3 Uniaxial three-point bending tests

The uniaxial three-point bending test was carried out on a Zwick 1456 testing machine (Zwick Roell GmbH &Co. KG, Ulm, Germany) according to the ČSN EN ISO 14125 standard. The results were evaluated using the TestXpert software. The distance between the supports was set to 60 mm, and the roundness of the supports and the load mandrel was 5 mm (Figure 2, scheme of the experimental design). The loading velocity was 50 mm/min. Samples were cut by a flex grinding machine GWS 7-125 (Robert Bosch, JSC, Gerlingen, Germany) in dimensions of (15 × 100 × 2) mm (width × length × thickness). Each measurement was repeated 10×, and mean values and standard deviations of the bending modulus of elasticity (E_B), upper yield point (F_{UY}), and elongation at upper yield point (dL_{FUY}) were determined. All experiments were performed at the ambient laboratory temperature of 25°C. A snapshot photograph of the used uniaxial tensile testing instrument in three-point bending test configuration is shown in Figure S3.

2.4 Charpy impact testing

Impact tests were carried out using a Zwick-Roell HIT25P machine (Zwick Roell, Ulm, Germany) according to the ČSN EN ISO 179-2 standard, allowing a 7.5 J energy drop. Samples were cut by a flex grinding machine GWS 7-125 (Robert Bosch, JSC, Gerlingen, Germany) in dimensions of (15 × 50 × 2) mm (width × length × thickness). Each experiment was repeated 10×, and mean values and standard deviations of the fracture toughness (a_k) and the absorbed impact work (W) were calculated. All experiments were performed at the ambient laboratory temperature of 25°C.

2.5 Displacement transmissibility measurements

The dynamic mechanical properties of the investigated specimens under harmonic loading were assessed by means of displacement transmissibility, denoted as T_d, and defined as follows [42]:

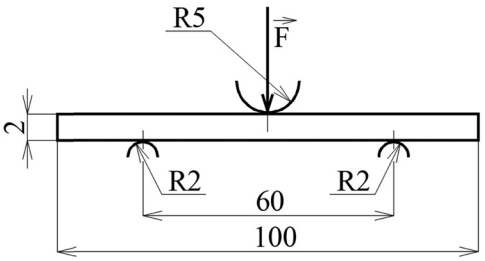

Figure 2: Scheme of the experimental setup for three-point bending tests.

$$T_d = \frac{y_2}{y_1} = \frac{a_2}{a_1}. \quad (1)$$

In this equation, y_1 is the displacement amplitude on the input side of the tested sample, while y_2 is the displacement amplitude on the output side of the tested sample. Similarly, a_1 is the acceleration amplitude on the input side of the tested sample, and a_2 is the acceleration amplitude on the output side of the tested sample. The displacement transmissibility of a spring–mass–damper system, consisting of components such as a spring with stiffness k, a damper with a damping coefficient c, and a mass m, is defined by the following equation [43]:

$$T_d = \sqrt{\frac{k^2 + (c\cdot\omega)^2}{(k - m\cdot\omega^2)^2 + (c\cdot\omega)^2}} = \sqrt{\frac{1 + (2\cdot\zeta\cdot r)^2}{(1 - r^2)^2 + (2\cdot\zeta\cdot r)^2}}. \quad (2)$$

When the zero value is reached by the derivative dT_d/dr in equation (2), the frequency ratio r_0 at which the maximum value of displacement transmissibility is attained can be determined [44,45]:

$$r_0 = \frac{\sqrt{\sqrt{1 + 8\cdot\zeta^2} - 1}}{2\cdot\zeta}. \quad (3)$$

Equation (3) clearly demonstrates that as the damping ratio ζ increases, or as the material's mechanical stiffness k decreases, the local extreme of the displacement transmissibility tends to shift towards lower frequency ratios r.

To conduct mechanical vibration tests, the forced oscillation method was applied. The displacement transmissibility, T_d, was quantified through experimental measurements. This was accomplished using a BK 4810 vibrator, in conjunction with a BK 3560-B-030 signal pulse multi-analyser and a BK 2706 power amplifier, spanning a frequency range from 2 to 1,600 Hz. The input and output sides of the test specimens were equipped with BK 4393 accelerometers (Brüel & Kjær, Nærum, Denmark) to record acceleration amplitudes a_1 and a_2.

The measurements of displacement transmissibility were conducted on test samples of the following dimensions: 15 mm in width, 60 mm in length, and 2 mm in thickness. These tests involved two inertial masses (m_i) weighing 90 and 300 g, respectively, placed on the top side of the tested specimens. Each measurement was repeated 10×, all conducted under ambient conditions at a temperature of 25°C.

2.6 Micro-hardness testing

Micro-indentation tests were performed on a micro-indentation tester (Micro Combi Tester, Anton Paar, Graz, Austria) according to the ČSN EN ISO 14577 standard. The applied diamond tip was cube-corner-shaped (Vickers, Anton Paar, Graz, Austria). Measurement parameters were set as follows: a maximum load of 3 N, a loading rate (unloading rate) of 6 N/min, and a holding time of 90 s. Samples were cut by a flex grinding machine GWS 7-125 (Robert Bosch, JSC, Gerlingen, Germany) in dimensions of (15 × 100 × 2) mm (width × length × thickness). All experiments were performed according to the depth sensing indentation method, allowing simultaneous measurement of the acting force on the indenter and the displacement of the indenter's tip. The embossing modulus (E_{IT}) was calculated from the plane strain modulus of elasticity (E^*) using an estimated Poisson's ratio (ν) of 0.35 for the studied samples [35,46]:

$$E_{IT} = E^*(1 - \nu^2) \quad (4)$$

The indentation hardness (H_{IT}) was measured as well. Each measurement was repeated 10×, and mean values and standard deviations of the indentation modulus were calculated. All experiments were performed at the ambient laboratory temperature of 25°C.

2.7 Shore D hardness measurements

Shore D hardness measurements were performed on an AFFRI Microhardness DM2D instrument (AFFRI, Inc., Wood Dale, IL, USA). The holding time was set to 4 s, and the applied method was "Shore D." Samples were cut by a flex grinding machine GWS 7-125 (Robert Bosch, JSC, Gerlingen, Germany) in dimensions of (15 × 100 × 2) mm (width × length × thickness). Each measurement was repeated 10×, and mean values and standard deviations of Shore D hardness were calculated. All experiments were performed at the ambient laboratory temperature of 25°C.

2.8 Statistical analysis

All experiments were repeated 10×. Experimental results were expressed as average values with standard deviations. SigmaPlot 12.5 software (Systat Software, Inc., San Jose, CA, USA) was used for the statistical analysis of data, and significance was determined through one-way analysis of variance (ANOVA) with a significance level set at $p < 0.05$. The normality of data distributions was confirmed using Shapiro–Wilk normality tests.

3 Results and discussion

3.1 SEM analysis and uniaxial tensile testing

Figure 3 depicts typical stress–strain patterns for the tested Samples 1 and 2 at a deformation rate of 5 mm/min. Three

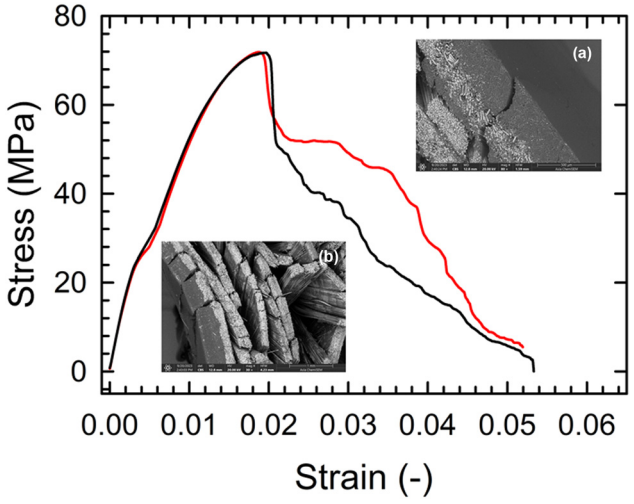

Figure 3: Results of the uniaxial tensile testing of studied materials at the 5 mm/min deformation rate: red line – sample 1, black line – sample 2. Insets: SEM images of the fracture surfaces of the tested samples (a – 80× magnification, b – 30× magnification).

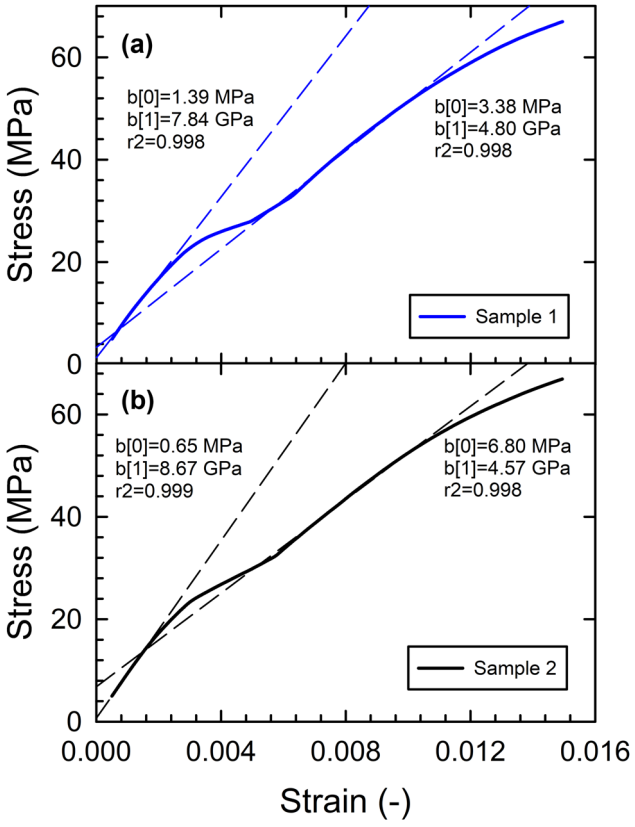

Figure 4: Details of the stress–strain dependencies of the studied materials observed at a 5 mm/min deformation rate. Inset: Parameters of the linear regression fittings of the tangents of the linear elastic parts: *b*[1] – Young's modulus of elasticity; *b*[0] – initial residual bias: (a) – sample 1, (b) – sample 2.

distinct deformation regions were clearly distinguished. The initial region corresponded to the linear elastic phase, typically observed for relative strains less than 0.02. An increase of 5% in the upper yield strain was observed for the GnP-reinforced composite compared to the virgin basalt epoxy specimen. However, this phase was characterized by the brittle fracture of both the epoxy matrix and the BF bundles, as confirmed by SEM analysis (Figure 3a inset).

Following the elastic region, a subsequent plastic deformation phase occurred, marked by the matrix's elongation and simultaneous frictional sliding of the fibres. This phase took place at relative strains ranging from 0.02 to 0.03.

Finally, a third debonding region was observed, where individual BF bundles were pulled out from the epoxy matrix, ultimately leading to specimen fracture (Figure 3b inset, SEM of the fracture surface). The step-like stress–strain pattern observed was attributed to the ongoing process of individual BF debonding.

Notably, in the low-strain elastic region, two consecutive linear elastic behaviour patterns were observed, as depicted in Figure 4. These patterns were modelled as the linear dependencies of the stress, represented as stress = $b[1] \times$ strain + $b[0]$. The observed Young's modulus of elasticity, denoted as $b[1]$, was found to be 7.84 GPa for virgin basalt-epoxy composites (Sample 1). However, in the case of graphene-modified matrices (Sample 2), the observed Young's modulus of elasticity increased to 8.67 GPa for lower strains. Conversely, for higher strains ranging from 0.004 to 0.016, a decreased Young's modulus of elasticity of 4.57 GPa was noted.

Based on these findings, it can be concluded that the first steeper tangent represents the Young's modulus of elasticity (E) of BFs, while the second tangent represents the E of the epoxy matrix, in alignment with the findings of Khalid *et al.* [47]. The obtained intercept magnitudes, $b[0]$, in the first elastic region were 1.39 MPa for Sample 1 and 0.65 MPa for Sample 2. These values indicated a slippage-induced bias dissipation mechanism in the graphene-modified specimens. This interpretation was based on the assumption that it follows a similar fashion to the case of the initial residual bias, which occurs due to pre-existing stress in samples resulting from the process of stretching and extending of the fabric material at an angle or direction not aligned with the primary warp and weft directions of the fabric [48].

Results of the uniaxial tensile testing at 10 mm/min deformation rate are shown in Figure 5 and Table 1. Young's modulus of elasticity (E) was increased to 11.25 GPa for Sample 1 and to 10.44 GPa for Sample 2 compared to the elastic moduli obtained for the 5 mm/min deformation rate. This confirmed a more rigid response of the matrix to the

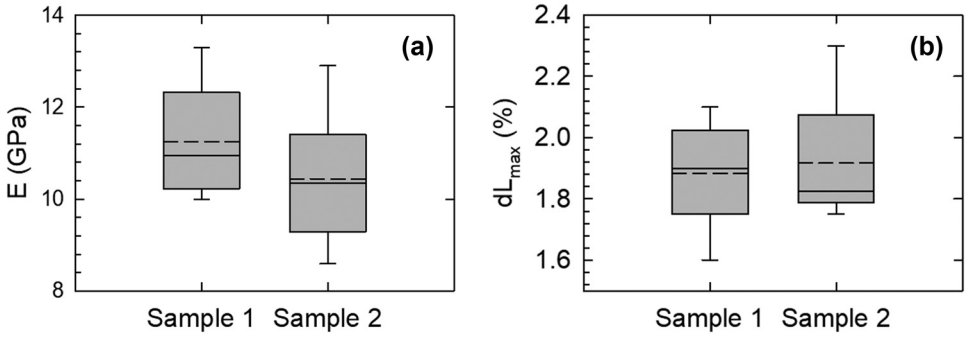

Figure 5: Results of uniaxial tensile testing for the studied samples at a deformation rate of 10 mm/min. (a) Young's modulus of elasticity. (b) Elongation at maximum tensile force. Box plot parameters: Long dashed lines indicate mean values, solid lines represent median values, and corresponding outliers. Obtained mean and median values of both parameters were not statistically significantly different as determined through one-way ANOVA ($p > 0.05$). Data match the pattern expected if the data were drawn from a population with a normal distribution as obtained by the Shapiro–Wilk normality test.

Table 1: Summary of the results of the measured quantities of the studied composite samples

Parameter	Sample 1	Sample 2
E (GPa)	11.25 ± 1.22^a	10.44 ± 1.45^a
dL$_{max}$ (%)	1.88 ± 0.17^a	1.92 ± 0.21^a
E_B (GPa)	12.86 ± 0.78^a	13.09 ± 0.57^a
dL$_{UY}$ (mm)	14.02 ± 1.32^a	14.23 ± 1.52^a
F_{UY} (N)	125.60 ± 9.05^a	134.90 ± 7.22^b
a_K (J/m^2)	125.19 ± 15.62^a	164.03 ± 20.81^b
W (J)	4.01 ± 0.50^a	5.25 ± 0.67^b
f_{R1} (m_i = 90 g) (Hz)	653.38 ± 21.25^a	706.42 ± 20.19^b
f_{R1} (m_i = 300 g) (Hz)	305.66 ± 10.12^a	411.37 ± 13.31^b
E_{IT} (GPa)	4.44 ± 0.09^a	4.25 ± 0.06^b
H_{IT} (MPa)	225.15 ± 7.12^a	211.16 ± 3.52^b
Shore D (–)	88.87 ± 1.67^a	86.25 ± 2.34^b

Differences in the mean values among the statistical groups were tested at a significance level of $p < 0.05$. The Tukey test was applied for multiple comparisons of the mean values to assess the statistical significance, *i.e.*, to evaluate if the differences were greater than what would be expected by chance; different superscript letters were used to indicate statistically significant differences between the values determined. The results were expressed as arithmetic mean ± standard deviation.

applied loads for measurements at 10 mm/min deformation rate. The obtained deformations at maximum force were higher in the case of Sample 2 (1.92%) compared to Sample 1 (1.88%). This was assumed to be due to the successful frictional sliding of GnPs proceeding within the complex composite matrix similar to that observed in carbon nanotubes' epoxy honeycomb sandwich panel composites [29].

3.2 Uniaxial three-point bending tests

The results of uniaxial three-point bending tests are presented in Figures 6 and 7. The observed bending modulus of elasticity increased from 12.86 GPa for Sample 1 to 13.09 GPa after the addition of planar GnPs into the composite structure (Figure 6a). This increase indicated a greater bending stiffness when subjected to perpendicular loading acting *via* the specimen's cross-section.

These effects were also reflected in the observed elongations at upper yield points (Figure 6b), which increased from 14.02 mm (Sample 1) to 14.23 mm (Sample 2).

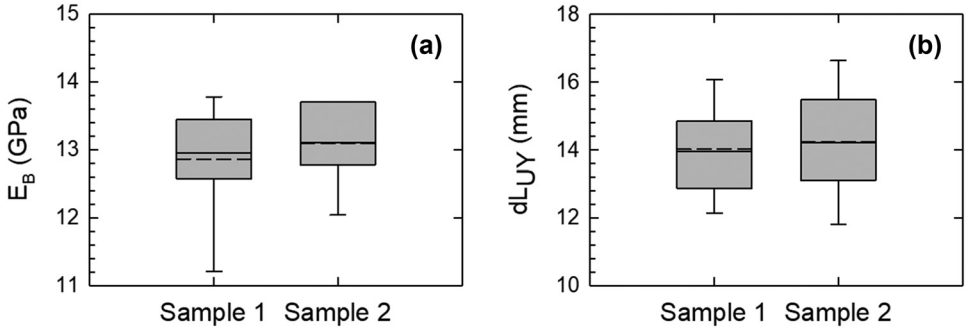

Figure 6: Results of uniaxial three-point bending tests for the studied composites (at a deformation rate of 50 mm/min). (a) Bending modulus of elasticity. (b) Elongation at the yield point. Box plot parameters: Long dashed lines indicate mean values, solid lines represent median values, and corresponding outliers. Obtained mean and median values of both parameters were not statistically significantly different as determined through one-way ANOVA ($p > 0.05$). Data match the pattern expected if the data were drawn from a population with a normal distribution as obtained by the Shapiro–Wilk normality test.

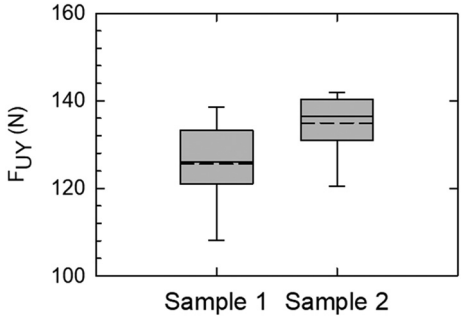

Figure 7: Force at the yield point obtained by the uniaxial three-point bending test of the studied composites. Box plot parameters: Long dashed lines indicate mean values, solid lines represent median values, and corresponding outliers. Obtained mean and median values of both parameters were statistically significantly different as determined through one-way ANOVA ($p < 0.05$). Data match the pattern expected if the data were drawn from a population with a normal distribution as obtained by the Shapiro–Wilk normality test.

Analogous to the previously discussed uniaxial tensile tests, it was proposed that this behaviour provided clear evidence of the continuous frictional sliding of the flat phases of the GnPs within the composite matrix. The hypothesized energy-dissipative pathways, relying on the latter-mentioned frictional sliding of GnPs and the simultaneous debonding and pull-out of BFs, were further substantiated by the increased forces observed at the upper yield points, increasing from 125.6 N (Sample 1) to 134.9 N (Sample 2), as illustrated in Figure 7 and detailed in Table 1.

3.3 Fracture toughness measurements

The results of fracture toughness measurements for the studied composites are presented in Figure 8 and Table 1. It is recognized that achieving high mechanical toughness in a material necessitates not only sufficient high material strength but also adequate deformability. The energy required to fracture the test specimen encompasses multiple components. In addition to the generation of new fracture surfaces, a significant portion of the hammer's energy is expended on viscoelastic or plastic deformations within the material surrounding the fracture surface or on the bending deformation of the entire test specimen. Another energy portion is converted into the kinetic energy of flying fragments or acoustic emissions or is absorbed by the testing equipment [49]. It was found that the graphene-reinforced Sample 2 exhibited an approximate 31% increase in fracture toughness (a_k = 164.03 J/m^2) compared to the unmodified Sample 1 (a_k = 125.17 J/m^2). A similar trend was also observed for the absorbed impact work, with a 31% increase as well (W = 5.25 J for Sample 2 and W = 4.01 J for Sample 1).

3.4 Vibration-excited dynamic mechanical testing

The results of the vibration-excited dynamic mechanical tests of the studied composite pipe's specimens are shown in Figure 9 and summarized in Table 1. The obtained frequency dependencies revealed distinct first resonant peak frequencies (f_{R1}) in the displacement transmissibility, reflecting the materials mechanical stiffness of the tested composites. It was observed in excellent agreement with equation (3) that higher f_{R1} values corresponded to the higher mechanical stiffness of the composite matrix [42,43]. Figure 9 illustrates that Sample 2 (with a GnP-modified matrix) consistently exhibited higher f_{R1} values, regardless of the applied inertial mass, compared to Sample 1 (with an unmodified composite matrix). This indicated that the

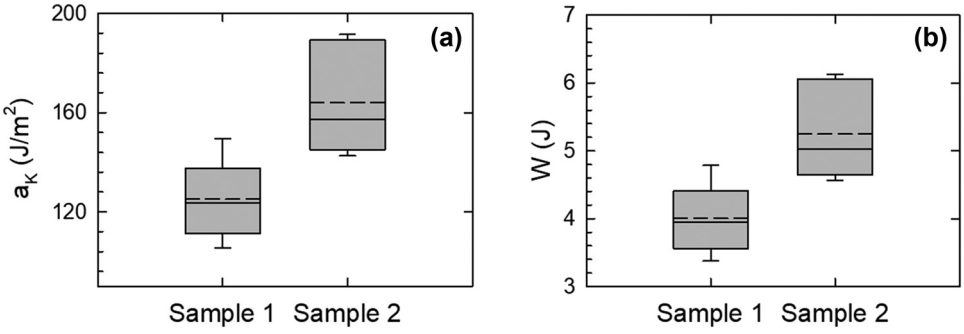

Figure 8: Results of Charpy pendulum impact tests for the studied composites. (a) Fracture toughness. (b) Absorbed impact work. Box plot parameters: Long dashed lines indicate mean values, solid lines represent median values, and corresponding outliers. Obtained mean and median values of both parameters were statistically significantly different as determined through one-way ANOVA ($p < 0.05$). Data match the pattern expected if the data were drawn from a population with a normal distribution as obtained by the Shapiro–Wilk normality test.

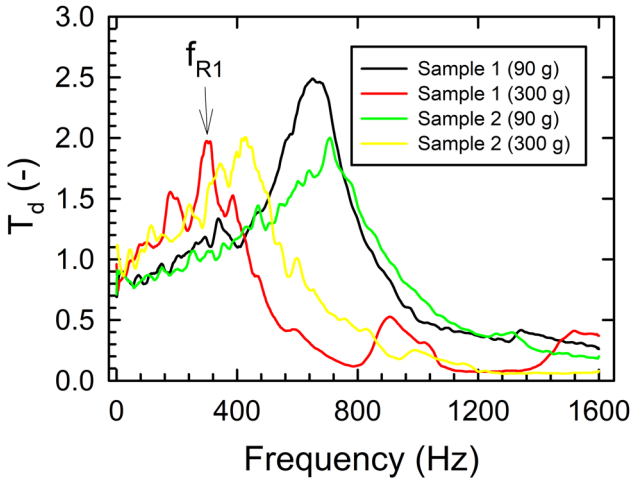

Figure 9: Frequency dependencies of the displacement transmissibility for the tested composites with applied inertial masses of 90 and 300 g.

addition of GnPs increased the mechanical stiffness of the composite matrix, making it suitable for applications in pipes subjected to high-pulsatile hydraulic pressure. A similar reinforcement effect was found for carbonaceous fillers in epoxy resin composites as well [29]. Therefore, these novel composites are excellent candidates for use in critical infrastructure or high-loaded pressurized components of tubular transport systems. Additionally, the increased mechanical stiffness of the GnP-reinforced composites led to higher durability [34], low weight, and simultaneous anticorrosive properties. The observed dynamic mechanical behaviour aligned positively with fracture toughness measurements, where the fracture toughness (a_k) increased when graphene was incorporated into the composite matrix structure.

Furthermore, a shift in f_{R1} towards lower excitation frequencies was observed with increasing inertial mass pre-loading of the specimen during dynamic mechanical vibrator testing. Because the natural frequency of the undamped system is proportional to the square root of the ratio of the material stiffness to the applied inertial mass [50], this leads to a decreasing dependence of the first resonance frequency with increasing inertial mass for each of the studied composites, as shown in Figure 9. This shift signifies that as the inertial mass increases, the system's tendency to vibrate at lower frequencies becomes more prominent. This effect plays a crucial role in energy damping mechanisms for vibration isolation. The lower frequency f_{R1} of the composite system at higher inertial mass suggests that the system is less inclined to vibrate at higher frequencies, resulting in increased stability. This trend is evident from Eq. (3), which shows that the local extreme of the displacement transmissibility generally shifts to lower values of the frequency ratio (r) as the damping ratio (ζ) increases or as the material stiffness (k) decreases.

3.5 Micro-hardness and Shore D hardness testing

The results of microhardness tests shown in Figure 10 confirmed the decrease of the measured indentation modulus (E_{IT}) after incorporation of the GnP filler into the composite matrix. E_{IT} decreased from 4.44 GPa (Sample 1) to 4.25 GPa (Sample 2). This behaviour was attributed to the plasticizing effect induced by the incorporated nanofillers within the composite matrix. These filler particles impacted the surface layers of the testing specimens. This assumption was further supported by the reduction in microhardness (H_{IT}), which decreased from 225.15 MPa (Sample 1) to 211.16 MPa (Sample 2). The obtained Shore D hardness of 86.25 of the graphene-modified Sample 2 was lower compared to the unmodified Sample 1 hardness of 88.87. This lower Shore D hardness reflected the same plasticizing effect of GnPs in the complex composite matrix as that observed in the microhardness measurements discussed above (Table 1).

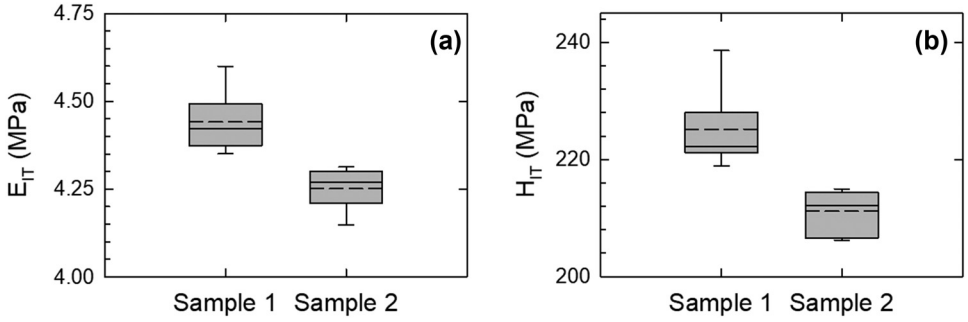

Figure 10: Results of micro-hardness measurements of the studied composites: (a) Embossing modulus (E_{IT}). (b) Indentation hardness (H_{IT}).

4 Conclusions

In this study, the increase in mechanical stiffness of basalt–epoxy composite pipes after incorporation of GnPs into the epoxy matrix was confirmed. An extensive set of experimental tests included uniaxial tensile tests, uniaxial three-point bending tests, fracture toughness measurements, vibration-induced dynamic mechanical tests, microhardness, and Shore hardness tests. The microstructure of the fracture surfaces was analysed by means of SEM. The simultaneous combination of fracture mechanisms initiated by the applied mechanical load, including the brittle fracture of the epoxy matrix, ductile fracture mechanisms such as BF separation, and internal friction of the GnPs, was confirmed. The results demonstrated changed material's mechanical properties, including Young's modulus of elasticity, elongation at break, hardness, mechanical stiffness and toughness, resulting from the incorporation of GnPs into the complex composite matrix. These changes were accompanied by observed plasticization effects, resulting in an approximate 2% increase in mechanical bending stiffness and a significant rise in fracture toughness from 125 to 164 J/m^2 (approximately 31%) in the composite tubular matrix. Additionally, there was an observed increase in dynamic mechanical stiffness from vibration damping tests of the GnP-modified epoxy composite pipe, making it suitable for a wide range of applications subjected to high-pulsatile hydraulic pressure. Therefore, these novel GnP-basalt–epoxy composites are excellent candidates for critical infrastructure or high-loaded pressurized tubular transport components.

Acknowledgments: MV expresses his gratitude for the financial support of this research through Project No. CZ.02.01.01/00/22_008/0004631 and "Materials and Technologies for Sustainable Development," within the Jan Amos Komensky Operational Program, funded by the European Union and the state budget of the Czech Republic. LL, BL, LK, and YM would like to extend their thanks for the funding provided by the Internal Grant of Palacky University in Olomouc (IGA_PrF_2023_024 and IGA_PrF_2024_020). Special thanks also due to Aleš Panáček (Palacky University Olomouc) for conducting SEM measurements.

Funding information: This research was funded by the project No. CZ.02.01.01/00/22_008/0004631, "Materials and Technologies for Sustainable Development," within the Jan Amos Komensky Operational Program, funded by the European Union and the state budget of the Czech Republic as well as by the Internal Grant of Palacky University in Olomouc (IGA_PrF_2023_024 and IGA_PrF_2024_020).

Author contributions: All authors have accepted responsibility for the entire content of this manuscript and approved its submission.

Conflict of interest: David Hui, who is the co-author of this article, is a current Editorial Board member of *Nanotechnology Reviews*. This fact did not affect the peer-review process. The authors declare no other conflict of interest.

Data Availability Statement: The data presented in this study are available on Zenodo 2022 https://zenodo.org/records/10819340 [55].

References

[1] Arikan H. Failure analysis of $(\pm 55°)_3$ filament wound composite pipes with an inclined surface crack under static internal pressure. Compos Struct. 2010 Jan;92(1):182–7.
[2] Avci A, Sahin Ö, Tarakcioglu N. Fatigue behavior of surface cracked filament wound pipes with high tangential strength in corrosive environment. Compos Part A-Appl Sci Manuf. 2007;38(4):1192–9.
[3] Fitriah SN, Majid M, Ridzuan M, Daud R, Gibson AG, Assaleh TA. Influence of hydrothermal ageing on the compressive behaviour of glass fibre/epoxy composite pipes. Compos Struct. 2017 Jan;159:350–60.
[4] Hawa A, Majid M, Afendi M, Marzuki H, Amin N, Mat F, et al. Burst strength and impact behaviour of hydrothermally aged glass fibre/epoxy composite pipes. Mater Des. 2016 Jan;89:455–64.
[5] Farshad M, Necola A. Effect of aqueous environment on the long-term behavior of glass fiber-reinforced plastic pipes. Polym Test. 2004 Apr;23(2):163–7.
[6] Kara M, Kirici M, Cagan SC. Effects of the number of fatigue cycles on the hoop tensile strength of glass fiber/epoxy composite pipes. J Fail Anal Prev. 2019 Aug;19(4):1181–6.
[7] Lu HF, Wu XN, Huang K. Study on the effect of reciprocating pump pipeline system vibration on oil transportation stations. Energies. 2018 Jan;11(1):132.
[8] tLato T, Mohany A. Passive damping of pressure pulsations in pipelines using Herschel-Quincke tubes. J Sound Vib. 2019 May;448:160–77.
[9] Wang Y, Shen TS, Tan CS, Fu J, Guo SR. Research status, critical technologies, and development trends of hydraulic pressure pulsation attenuator. Chin J Mech Eng. 2021 Jan;34(1):14.
[10] Suhane A. Experimental study on centrifugal pump to determine the effect of radial clearance on pressure pulsations, vibrations and noise. Int J Eng Res Appl. 2012;2(4):1823–9.
[11] Lapcík L, Vasina M, Lapcíková B, Burecek A, Hruzík L. Effect of rapeseed oil on the rheological, mechanical and thermal properties of plastic lubricants. Mech Time-Depend Mater. 2022 Mar;26(1):33–47.
[12] Militky J, Kovacic V, Bajzík V. Mechanical properties of basalt filaments. Fibres Text East Europe. 2007;15(5–6):49–53.
[13] Dhand V, Mittal G, Rhee KY, Park SJ, Hui D. A short review on basalt fiber reinforced polymer composites. Compos Part B-Eng. 2015 May;73:166–80.
[14] Tao WC, Wang B, Wang NX, Guo YF, Li JY, Zhou ZW. Research progress on basalt fiber-based functionalized composites. Rev Adv Mater Sci. 2023 Mar;62(1):20220300.

[15] Chen XF, Zhang YS, Hui D, Chen MR, Wu ZS. Study of melting properties of basalt based on their mineral components. Compos Part B-Eng. 2017 May;116:53–60.
[16] Sim J, Park C, Moon DY. Characteristics of basalt fiber as a strengthening material for concrete structures. Compos Part B-Eng. 2005;36(6–7):504–12.
[17] Wang MC, Zhang ZG, Li Y, Li M, Sun ZJ. Chemical durability and mechanical properties of alkali-proof basalt fiber and its reinforced epoxy composites. J Reinf Plast Compos. 2008;27(4):393–407.
[18] Dalinkevich AA, Gumargalieva KZ, Marakhovsky SS, Soukhanov AV. Modern basalt fibrous materials and basalt fiber-based polymeric composites. J Nat Fibers. 2009;6(3):248–71.
[19] Shiu SC, Tsai JL. Characterizing thermal and mechanical properties of graphene/epoxy nanocomposites. Compos Part B-Eng. 2014 Jan;56:691–7.
[20] Wu ZS, Wang X, Iwashita K, Sasaki T, Hamaguchi Y. Tensile fatigue behaviour of FRP and hybrid FRP sheets. Compos Part B-Eng. 2010 Jul;41(5):396–402.
[21] Pascault J, Williams RJ. Epoxy polymers: New materials and innovations. Hoboken, NJ, USA: John Wiley & Sons; 2009.
[22] Zakaria MR, Kudus M, Akil HM, Thirmizir M. Comparative study of graphene nanoparticle and multiwall carbon nanotube filled epoxy nanocomposites based on mechanical, thermal and dielectric properties. Compos Part B-Eng. 2017 Jun;119:57–66.
[23] Lopresto V, Leone C, De Iorio I. Mechanical characterisation of basalt fibre reinforced plastic. Compos Part B-Eng. 2011 Jun;42(4):717–23.
[24] Wei B, Cao HL, Song SH. Degradation of basalt fibre and glass fibre/epoxy resin composites in seawater. Corros Sci. 2011 Jan;53(1):426–31.
[25] Wang X, Wu ZS, Wu G, Zhu H, Zen FX. Enhancement of basalt FRP by hybridization for long-span cable-stayed bridge. Compos Part B-Eng. 2013 Jan;44(1):184–92.
[26] Kausar A, Ahmad I. Leading-edge polymer/carbonaceous nano-reinforcement nanocomposites-opportunities for space sector. Adv Mater Sci. 2023 Dec;23(4):99–122.
[27] Najmi L, Hu Z. Effects of topological parameters on thermal properties of carbon nanotubes *via* molecular dynamics simulation. J Compos Sci. 2024 Jan;8(1):37.
[28] Najmi L, Hu Z. Review on molecular dynamics simulations of effects of carbon nanotubes (CNTs) on electrical and thermal conductivities of CNT-modified polymeric composites. J Compos Sci. 2023 Apr;7(4):165.
[29] Najmi L, Zebarjad SM, Janghorban K. Effects of carbon nanotubes on the compressive and flexural strength and microscopic structure of epoxy honeycomb sandwich panels. Polym Sci Ser B. 2023 Apr;65(2):220–9.
[30] Sepetcioglu H, Tarakcioglu N, Rafiee R. Experimental investigation of graphene nanoplatelets effect on the fatigue behavior of basalt/epoxy composite pressure vessels. Thin-Walled Struct. 2022 Feb;171:108672.
[31] Urade AR, Lahiri I, Suresh KS. Graphene properties, synthesis and applications: A review. JOM. 2023 Mar;75(3):614–30.
[32] Zhang B, Asmatulu R, Soltani SA, Le LN, Kumar S. Mechanical and thermal properties of hierarchical composites enhanced by pristine graphene and graphene oxide nanoinclusions. J Appl Polym Sci. 2014 Oct;131(19):40826.
[33] Du XS, Zhou H, Sun WF, Liu HY, Zhou GN, Zhou HM, et al. Graphene/epoxy interleaves for delamination toughening and monitoring of crack damage in carbon fibre/epoxy composite laminates. Compos Sci Technol. 2017 Mar;140:123–33.
[34] Sepetcioglu H, Demet SM, Bagci M. A comprehensive experimental study of enhanced solid particle erosive resistance on the inner/outer surface of graphene nanoplatelets modified basalt/epoxy composite pipe. Polym Compos. 2023;44(10):6944–56.
[35] Oliver WC, Pharr GM. Measurement of hardness and elastic modulus by instrumented indentation: Advances in understanding and refinements to methodology. J Mater Res. 2004 Jan;19(1):3–20.
[36] Madhukar MS, Drzal LT. Fiber-matrix adhesion and its effect on composite mechanical properties.1. Inplane and interlaminar shear behavior of graphite epoxy composites. J Compos Mater. 1991 Aug;25(8):932–57.
[37] Bulut M. Mechanical characterization of Basalt/epoxy composite laminates containing graphene nanopellets. Compos Part B-Eng. 2017 Aug;122:71–8.
[38] Boehm HP. Graphene-How a laboratory curiosity suddenly became extremely interesting. Angew Chem-Int Ed. 2010;49(49):9332–5.
[39] Molak RM, Kartal M, Pakiela Z, Manaj W, Turski M, Hiller S, et al. Use of micro tensile test samples in determining the remnant life of pressure vessel steels. Adv Exp Mech V. 2007;7–8(5):187–+.
[40] El-Bagory T, Younan M, Sallam H. Mechanical behavior of welded and un-welded polyethylene pipe materials. Proceedings of the ASME Pressure Vessels and Piping Conference 2013, Vol. 6B: Materials and Fabrication. 2013, 2014.
[41] Stamenovic M, Putic S, Rakin M, Medjo B, Cikara D. Effect of alkaline and acidic solutions on the tensile properties of glass-polyester pipes. Mater Des. 2011 Apr;32(4):2456–61.
[42] Lapcik L, Vasina M, Lapcikova B, Stanek M, Ovsik M, Murtaja Y. Study of the material engineering properties of high-density poly(ethylene)/perlite nanocomposite materials. Nanotechnol Rev. 2020 Jan;9(1):1491–9.
[43] Lapcík L, Sepetcioglu H, Murtaja Y, Lapcíková B, Vasina M, Ovsík M, et al. Study of mechanical properties of epoxy/graphene and epoxy/halloysite nanocomposites. Nanotechnol Rev. 2023 Mar;12(1):20220520.
[44] Carrella A, Brennan MJ, Waters TP, Lopes V Jr. Force and displacement transmissibility of a nonlinear isolator with high-static-low-dynamic-stiffness. Int J Mech Sci. 2012;55(1):22–9.
[45] Ab Latif N, Rus AZM. Vibration transmissibility study of high density solid waste biopolymer foam. J Mech Eng Sci. 2014;6:772–81.
[46] Manas D, Mizera A, Manas M, Ovsik M, Hylova L, Sehnalek S, et al. Mechanical properties changes of irradiated thermoplastic elastomer. Polymers. 2018 Jan;10(1):87.
[47] Khalid FS, Irwan JM, Ibrahim M, Othman N, Shahidan S. Splitting tensile and pullout behavior of synthetic wastes as fiber-reinforced concrete. Constr Build Mater. 2018 May;171:54–64.
[48] Boisse P, Hamila N, Guzman-Maldonado E, Madeo A, Hivet G. dell'Isola F. The bias-extension test for the analysis of in-plane shear properties of textile composite reinforcements and prepregs: A review. Int J Mater Form. 2017 Aug;10(4):473–92.
[49] Lapcik L, Raab M. Materials science II. Textbook. Zlin, Tomas Bata University in Zlin. 2nd edn. Zlin: Tomas Bata University in Zlin; 2004.
[50] Lapcik L, Manas D, Lapcikova B, Vasina M, Stanek M, Cepe K, et al. Effect of filler particle shape on plastic-elastic mechanical behavior of high density poly(ethylene)/mica and poly(ethylene)/wollastonite composites. Compos Part B-Eng. 2018 May;141:92–9.